



Investigation of tyre rim protectors on the aerodynamics of a passenger vehicle

Downloaded from: <https://research.chalmers.se>, 2025-06-24 04:03 UTC

Citation for the original published paper (version of record):

Josefsson, E., Semeraro, F., Urquhart, M. et al (2024). Investigation of tyre rim protectors on the aerodynamics of a passenger vehicle. *Experiments in Fluids*, 65(5).
<http://dx.doi.org/10.1007/s00348-024-03805-0>

N.B. When citing this work, cite the original published paper.



Investigation of tyre rim protectors on the aerodynamics of a passenger vehicle

Erik Josefsson¹ · Francesco Fabio Semeraro² · Magnus Urquhart³ · Simone Sebben¹

Received: 25 August 2023 / Revised: 29 January 2024 / Accepted: 26 March 2024 / Published online: 10 April 2024
© The Author(s) 2024

Abstract

The wheels of a passenger vehicle contribute to a significant part of the vehicle's aerodynamic drag. The previous research has shown that the flow is sensitive to small geometrical variations of the tyre, such as its shoulder profile and tread pattern. This work investigates the effect of altering the tyre profile in the transition region between the tyre and the rim by adding a so-called rim protector. Full-scale wind tunnel tests capturing forces, flow fields and surface pressures were conducted for three tyre variants in combination with two rim configurations on a crossover SUV. With a low rim protector, the forces and flow fields were similar to the reference tyre without a rim protector for both rims. With a wide, protruding, rim protector on the open rim, a larger and more outwashed front wheel wake was obtained with differences in the vortex structures, resulting in a drag penalty of $0.017 C_D$. The altered front wheel wake reduced the shielding of the rear wheel, resulting in differences in the rear wheel wake and base pressure. With a closed rim, the differences with the wide rim protector were much smaller with only a slight drag increase compared to the reference, demonstrating that there can be a strong interaction between the tyre and rim design.

1 Introduction

The aerodynamic drag is one of the largest resistive forces acting on a passenger vehicle (Schuetz 2015), affecting its energy efficiency and resulting driving range. Thus, in the automotive industry, there is a need for a better understanding of how the drag is formed and how it can be reduced. A considerable part of the vehicle drag originates from the wheels, making it a subject of increased research in the past years. The rotation of the wheels, the deformation of the

tyres and the interaction between the tyre and rim create a complex flow that is challenging to understand.

Wickern et al. (1997) demonstrated that by removing the wheels and covering the wheelhouses, the drag was reduced by 25%, thus quantifying the large impact of the wheels. Although this cannot be done for an actual vehicle, later studies have shown that significant drag reductions can be found depending on the wheel design. Much of the previous research, such as Koitrant et al. (2015), Schnepf et al. (2015) and Brandt et al. (2019), focused on the design of the rim, finding that the coverage area is one of the most important factors for reducing the drag. Landström et al. (2012) proved that also the tyre can substantially alter the drag, with variations of 0.005 – $0.010 C_D$ between similar tyres with the same specified dimension. The sensitivity of different tyre parameters, such as the profile (Wittmeier et al. 2014), deformation (Mlinaric 2007; Gray et al. 2019) and tread pattern (Mercker et al. 1991; Wickern et al. 1997; Hobeika and Sebben 2018), has been further investigated, all resulting in modifications of the flow around the wheel.

Some tyre features have received less attention in the previous research. One of them is the transition region between the tyre and the rim. Commercial tyres are commonly equipped with a so-called *rim protector* (or rim shield), typically added to the tyre's outer edge and designed to protect

✉ Erik Josefsson
erik.josefsson@chalmers.se

Francesco Fabio Semeraro
francescofabio.semeraro@polimi.it

Magnus Urquhart
magnus.urquhart@volvocars.com

Simone Sebben
simone.sebben@chalmers.se

¹ Department of Mechanics and Maritime Sciences, Chalmers University of Technology, 412 96 Gothenburg, Sweden

² Department of Mechanical Engineering, Politecnico di Milano, 201 56 Milan, Italy

³ Aerodynamics, Volvo Cars, 418 78 Gothenburg, Sweden

the rim from damage by, for example, a curb or during wheel handling. Wittmeier et al. (2013) compared several tyres fitted to a range of vehicles and found that the tyre with a rim protector resulted in increased drag for all vehicle types. In a study of isolated wheels, Reiß et al. (2020) found that the tyre with a rim protector performed worse than the other configurations analysed. However, in both Wittmeier et al. (2013) and Reiß et al. (2020), the tyres with the rim protectors also featured additional differences from the other configurations. Hence, the effect of the rim protector itself could not be isolated.

This work investigates the impact of rim protectors using full-scale wind tunnel measurements, capturing forces, flow fields and surface pressures. The tyres were specifically designed by Pirelli and only varied in the rim protector region. The tests were conducted with two rim configurations on a crossover SUV.

2 Methodology

2.1 Vehicle geometry

The Volvo C40 Recharge was tested with closed front cooling inlets. Two rim configurations were studied, open and closed, Fig. 1. The closed rim was obtained by attaching a 2 mm thick carbon fibre sheet to the outside of the open rim. The cover was convex, extending 28 mm out from the rim edge (21 mm outside the wide rim protector) at the wheel centre. Where applicable, the cover is also illustrated along with the measurements. Due to brake cooling requirements, a completely closed rim is not feasible for an actual vehicle. It does, however, reflect current trends in the vehicle industry (Koitrant et al. 2015; Schnepf et al. 2015; Brandt et al. 2019; Barth et al. 2020).

Three sets of 245/45 R19 tyres were tested, a reference tyre with no rim protector along with a low and a wide rim protector variant (Fig. 2). Apart from the rim protectors, the tyres were identical and featured the same detailed tread pattern and shoulder profile. The same tyre and rim

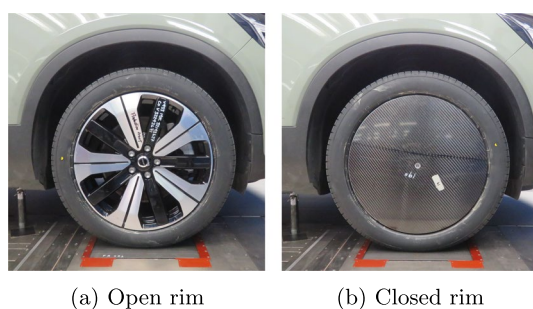


Fig. 1 Investigated rim configurations

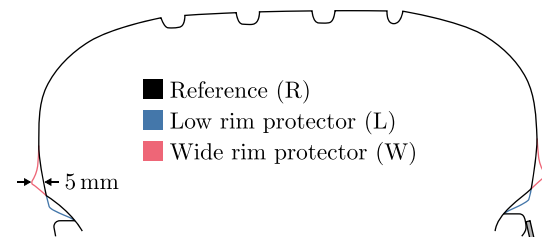


Fig. 2 Cross-sections of the tyres. The thickness of the rim cover is illustrated in grey in the bottom right corner

configuration was used for all four wheels. The vehicle's frontal area was kept constant at 2.54 m^2 for all calculations as any differences caused by the rim protector or rim cover were small.

2.2 Wind tunnel

The experiments were performed in the Volvo Cars Aerodynamic Wind Tunnel (PVT), which is described in detail by Sternéus et al. (2007). The tunnel has a slotted wall test section with a cross-sectional area of 27.1 m^2 , resulting in a blockage of 9.4% with the current vehicle. PVT is equipped with a ground effect simulation system consisting of a scoop, two distributed suction zones and a five-belt system with a centre belt and four wheel drive units (WDUs), Fig. 3. Their exposed area is tangential to the ground and measures $400 \times 360 \text{ mm}$. The flat surface of the WDUs results in realistic contact patches for the tyres. The WDUs were placed such that the contact patch was centred on the belt. The

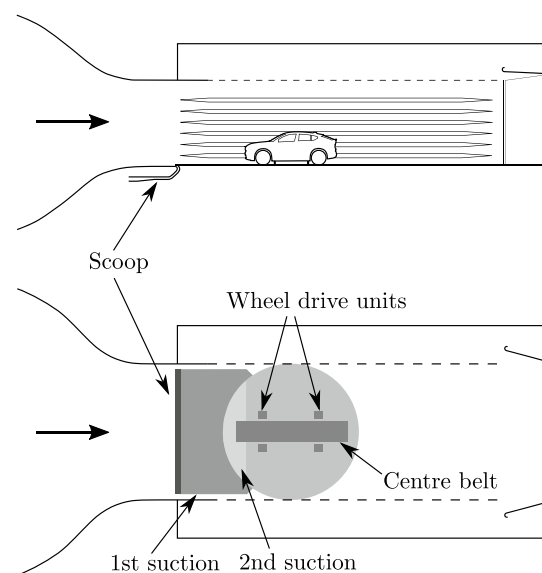


Fig. 3 Layout of the boundary layer control system in PVT drawn to scale. Adapted from Ljungskog et al. (2019)

Table 1 Force coefficient 95% uncertainty estimations. The base drag is calculated from the pressure measurements, as described in Sect. 2.4

Force	Coefficient	Uncertainty
Drag	C_D	± 0.0011
Front lift	C_{LF}	± 0.0006
Rear lift	C_{LR}	± 0.0013
Base drag	C_{DB}	± 0.0013

test object was held in place by four rocker panel restraint posts with a diameter of 36 mm. All measurements were performed at 100 km/h.

2.3 Force measurements

The forces were captured by the underfloor balance and averaged for 40 s. All measurements were conducted during the same test campaign, mitigating the uncertainty due to mounting of the vehicle in the wind tunnel. The uncertainties of the force coefficients were determined from ten individual measurements of the same configuration and are presented in Table 1. Since the results of this work will be presented in terms of force deltas, the uncertainties in Table 1 are combined using the root sum squared method, resulting in scaling by $\sqrt{2}$.

2.4 Pressure measurements

The vehicle was equipped with pressure spades at the right-hand side of the base. The pressures were sampled by First Sensor HCLA0025DB units connected to Dewesoft Sirius modules at 5000 Hz for 60 s. The sensors had a range of ± 2500 Pa and were statically calibrated to within ± 5 Pa ($0.01 C_p$ at 100 km/h). The averaging time was sufficient to achieve a 95% uncertainty of less than $\pm 0.003 C_p$ for all sensors. Due to the length of the pressure tubing, only the averaged values are considered here.

The base pressure was integrated over the measurement area to determine the base drag coefficient, C_{DB} . Since measurements were only taken at half the base, the value was multiplied by two to correspond to the full vehicle. This should be valid since the car is mostly symmetrical, as confirmed by symmetrical yaw sweeps with negligible side force at zero yaw. Performing repeated measurements of the same configuration, the uncertainty for the base drag was found to be $\pm 0.0013 C_{DB}$, as presented in Table 1.

2.5 Flow field measurements

Flow field measurements were taken using the traversing gear and two 12-hole Omniprobes mounted with a vertical spacing of 56 mm. The probes measure the flow within $\pm 150^\circ$, and, to better capture the recirculating flows in wakes, they were placed at 45° to the freestream. Using the manufacturer's calibration, the 12 pressures were used to calculate the velocity vector along with the static and total pressures. The probes had a specified accuracy of 3% and 1.5° in terms of velocity magnitude and flow angle, respectively (Aeroprobe corporation 2015).

The captured planes are shown in Fig. 4, where FW and RW denote front and rear wheel. Both FW x and RW x were located 500 mm downstream of the corresponding wheel axle. FW y was placed 25 mm outside of the tyre bulge. FW z was taken 25 mm from the ground, whereas RW z was placed 80 mm above the ground to avoid measuring mostly the boundary layer built up along the wind tunnel floor. The base plane was 100 mm behind the rearmost part of the car, corresponding to approximately 500 mm downstream of RW x .

The Γ_2 criteria, proposed by Graftieaux et al. (2001), were used to illustrate vortices. Although Γ_2 does not convey information about the strength of the vortices, only about their size and positioning, it was found preferable to quantities such as vorticity or the Q -criteria since it is less sensitive to noise (De Gregorio and Visingardi 2020). The rotation of the flow is described by first constructing the average velocity in a region S around a point P as

$$\vec{v}_P = \frac{1}{N} \sum_{M \in S} \vec{v}_M. \quad (1)$$

Next, Γ_2 is calculated as

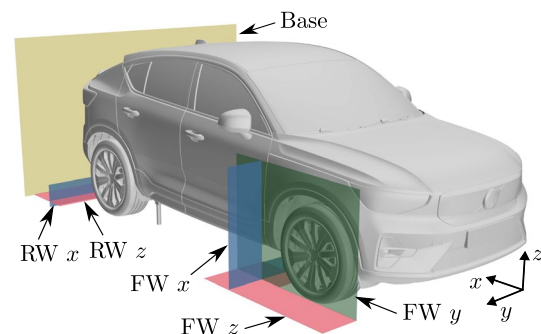


Fig. 4 Planes used for flow field measurements

$$\begin{aligned}\Gamma_2 &= \frac{1}{N} \sum_{M \in S} \frac{[\overrightarrow{PM} \times (\vec{v}_M - \vec{v}_P)] \cdot \hat{n}}{\|\overrightarrow{PM}\| \cdot \|\vec{v}_M - \vec{v}_P\|} \\ &= \frac{1}{N} \sum_{M \in S} \sin \theta_{PM},\end{aligned}\quad (2)$$

with \hat{n} being the plane normal and M the other points in S . Graphically, this can be interpreted as the average of $\sin \theta_{PM}$, as illustrated in Fig. 5. In this work, S was taken as a disc centred around P . The radius was chosen as a compromise between resolution and spatial averaging. For the planes FW x and RW x , the radius was 50 mm, whereas 200 mm was used for the base plane.

The measurements were conducted by sweeping the probes at 40 mm/s and sampling the pressures at 20 Hz. The measurement lines were spaced 28 mm apart for all planes except the base plane, which used a spacing of 56 mm. The sweeping method is much faster than the traditional method of stopping the traverse and sampling at discrete points. Ten measurements of the bottom part of the FW x plane were taken to investigate the repeatability of the method. Figure 6 shows the average total pressure coefficient and Γ_2 from the ten measurements along with isolines from the individual measurements at $C_{ptot} = 0$ and $|\Gamma_2| = 0.4$. The value for Γ_2 was chosen arbitrarily to illustrate the repeatability. All measurements result in similar isolines, indicating that the repeatability is sufficient for comparing the flow fields of different tyres.

The traverse is known to introduce a disturbance in the flow. Previous investigations, using the same wind tunnel and equipment, showed that although the flow can be somewhat altered (Sterken et al. 2014; Josefsson 2022), the flow structures are still qualitatively similar.

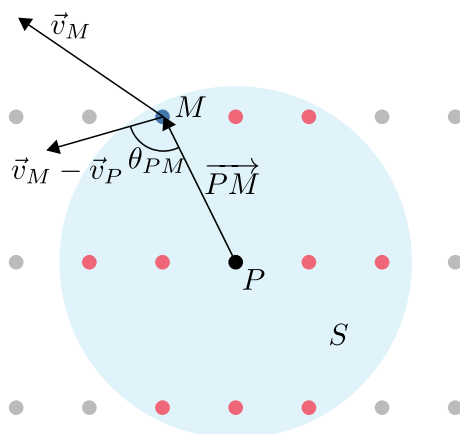


Fig. 5 Calculation of Γ_2 around a point P in region S . Inspired by Parfett et al. (2022)

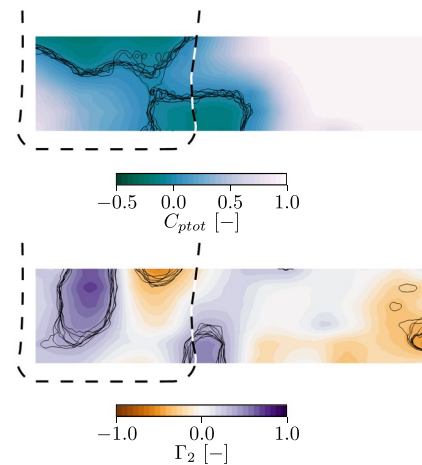


Fig. 6 Average field and individual isolines from ten repeated measurements in the lower part of the FW x plane. The isolines are drawn at $C_{ptot} = 0$ and $|\Gamma_2| = 0.4$. The dashed line marks the contour of the wheel

3 Results

3.1 Force measurements

Figure 7 shows the force coefficient deltas compared to the reference tyre (R) with the open rim and R with the closed rim, respectively. With the open rim, no significant drag difference is measured for the low rim protector (L) but a $0.017 C_D$ increase is obtained for the wide rim protector (W), corresponding to approximately 5% of the total drag. The base drag coefficient, C_{DB} , indicates that only a small part of this difference occurs at the base, suggesting that the main changes happen locally around the wheels. With the closed rim, the large drag difference between R and W vanishes, showing that there is a strong interaction

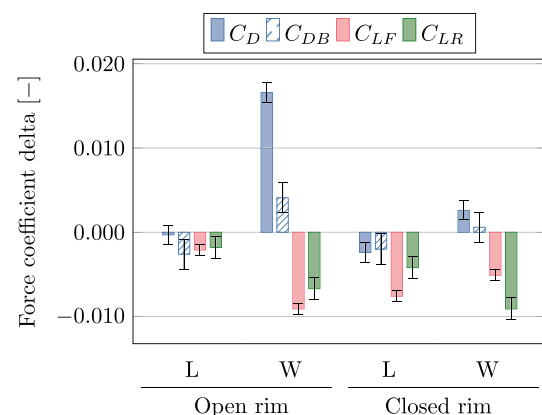


Fig. 7 Force coefficient deltas compared to the reference tyre (R) on the open and closed rims, respectively

between tyre and rim design. A slight drag reduction of approximately the same size as the base drag delta is measured for L. More consistent results are seen for the lift forces, where the two rim protector variants reduce front and rear lift compared to the reference.

3.2 Rim protectors on the open rim

3.2.1 Front wheel flow

Figure 8 illustrates Γ_2 and total pressure coefficient in the FW x plane for the three tyres with the open rim. The investigated vortices and their corresponding low-energy regions are labelled according to the nomenclature used in Josefsson et al. (2022, 2023). Starting with the reference tyre (R), a

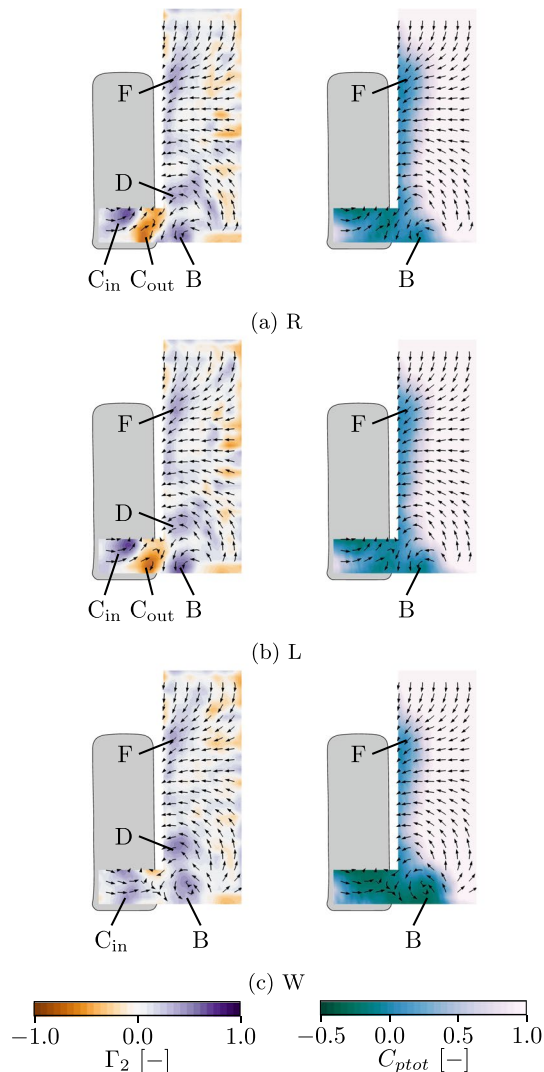


Fig. 8 Flow field measurements in the FW x plane for the three tyres with the open rim

region of positive Γ_2 , corresponding to the counterclockwise rotating outer contact patch vortex (B), is measured along with a matching low-energy region in C_{ptot} . Right downstream of the tyre there is a pair of counter-rotating vortices, C_{in} and C_{out} , resulting from the separation at the aft tyre shoulders. They cause a slight upwash in the otherwise outwash-dominated region. The upwash results in flow entering the rear part of the front wheelhouse. The leakage from the top of the wheelhouse produces vortex F and a corresponding low-energy region. Above B there is another counterclockwise rotating vortex, D, created from the separation at the rim flange, as described by Wäschle (2007).

Comparing the reference (R) and the low rim protector (L), no significant differences are seen, Fig. 8b. Since the results with L are very similar to those of R, the figures for L will be omitted from here on, unless they are necessary for the explanation. With the wide rim protector (W), the outer contact patch vortex (B) is larger, Γ_2 in Fig. 8c. This results in the larger low-energy region seen in C_{ptot} , likely explaining part of the drag increase presented in Fig. 7. A larger C_{in} is obtained, showing that the wide rim protector also alters the separation at the inner tyre shoulder. Due to the larger B and C_{in} , C_{out} is not visible in this plane. Without C_{out} , the upwash in the wake of the reference tyre diminishes, and an outwash is created instead. This means that less flow enters the rear part of the wheelhouse, leading to less leakage from the wheelhouse top and, thus, a smaller upper separation (F), as visible in the total pressure plots. As illustrated by Γ_2 , vortex D is larger than for the other tyres. Wäschle (2007) attributed this vortex to the separation at the

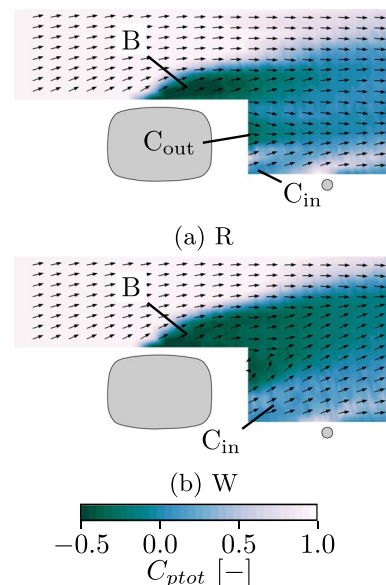


Fig. 9 Flow field measurements in the FW z plane with the open rim. For reference, the outline of the mounting strut is indicated

rim flange. Although the separation here occurs at the rim protector, the effect is the same.

Figure 9 presents the total pressure coefficient in the FW z plane. There are distinct low-energy regions corresponding to vortices B, C_{in} and C_{out} visible for R. With W, both the size and intensity of the low-energy regions increase. As was observed in the FW x plane, there is more outwash than for R, altering the direction of the wake.

The spanwise velocity in the planes FW x and FW y is plotted in Fig. 10. In FW x , the outflow behind the tyre is visible. Due to C_{out} (Fig. 8a and 8b), the region of $v_y = 0$ behind the tyre (labelled 1 in Fig. 10a) is slanted for R. With W, the altered vortex structure gives more outwash close to the ground. Comparing R to W in the FW y plane, the largest differences are observed in the region close to the ground that is not shielded by the wheelhouse. With W, there is more outflow along the upstream tyre shoulder (2). There is a region of $v_y \approx 0$ in the downstream transition between the rim and tyre (3), showing that the flow is forced outwards by the wide rim protector. In the upper part of the FW y plane, the difference in leakage from the wheelhouse, discussed in connection to Fig. 8, is visible (4).

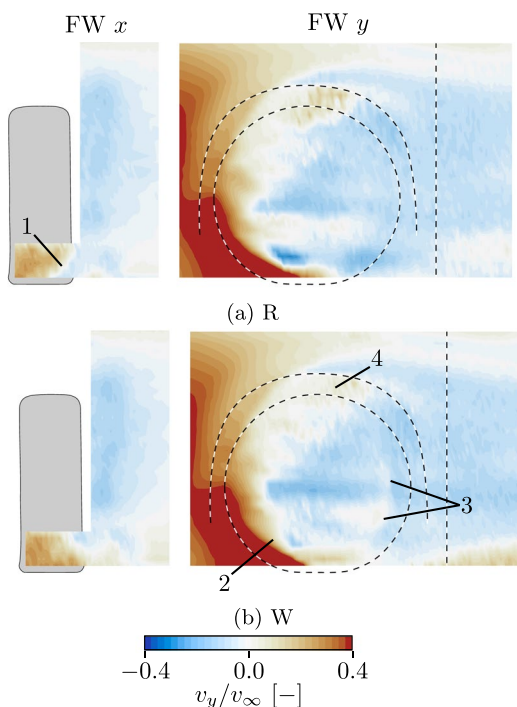


Fig. 10 Normalised spanwise velocity in the planes FW x and FW y for the open rim. Positive values correspond to flow out from the vehicle. The dashed lines in FW y mark the outline of the wheel and wheelhouse as well as the location of the FW x plane

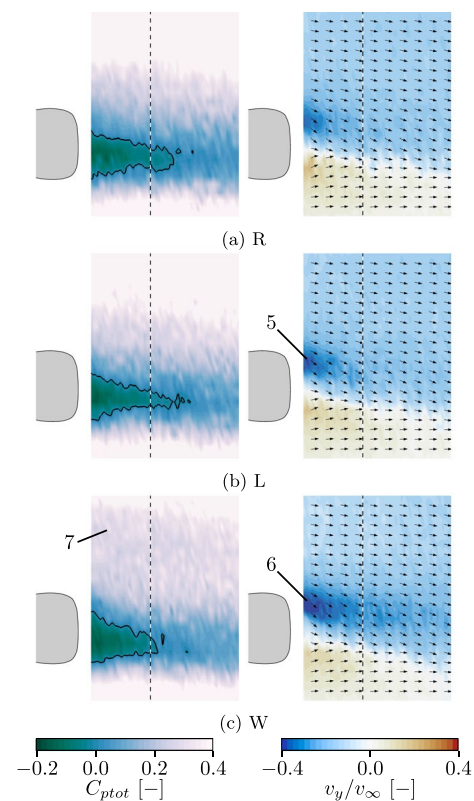


Fig. 11 Flow field measurements in the RW z plane with the open rim. Isolines are drawn for $C_{ptot} = 0$, and the dashed line marks the location of the RW x plane

3.2.2 Rear wheel flow

Figure 11 shows the flow at the rear right wheel in the RW z plane. R and L are again similar but a slightly narrower low-energy region and more inwash at the outer tyre shoulder (5) are measured with L. This could indicate that the low rim protector improves the transition between the tyre and the rim. An even stronger inflow is observed downstream of W, 6 in Fig. 11c. The resulting wake is shorter than for R. However, the losses are larger for W, especially close to the tyre. Far outside of the tyre (7 in Fig. 11c), the extent of the larger and more outwashed front wheel wake of W can be seen. The previous research has shown that the flow structures from the front wheel alter the flow around the rear wheel (Josefsson et al. 2023; Radovic et al. 2023). With the more outwashed front wheel wake of W, the rear wheel is likely less shielded from the freestream flow, potentially explaining the larger losses in the rear wheel wake.

To explain the difference in inflow behind the rear wheels, the vortex structures in the RW x plane are visualised, Fig. 12. The strong inwash with W observed in Fig. 11c can

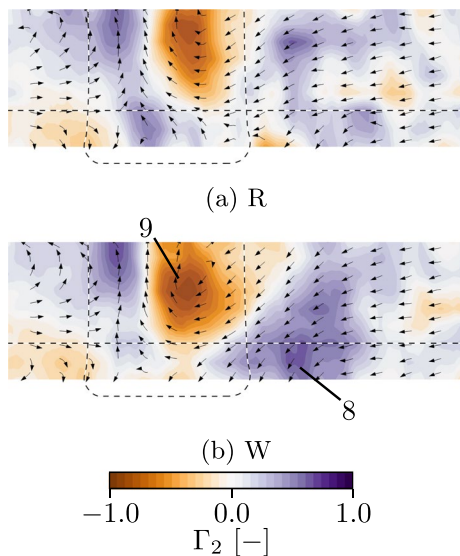


Fig. 12 Vortex structures in the RW x plane with the open rim. The dashed lines mark the outline of the tyre and the RW z plane

be connected to a counterclockwise rotating structure (8) present only for W. It is likely the outer contact patch vortex of the rear wheel and is not visible for R. This could be explained by the difference in the tyre geometry, but also by that the shielding from the front wheel wake results in lower energy flow upstream of the rear wheels for R. The clockwise rotating structure (9) is larger for W, further enhancing the inflow.

Figure 13 presents the base pressure of R and the corresponding base pressure deltas of L and W. With L, the base pressure is generally higher, resulting in the marginally lower C_{DB} presented in Fig. 7. This difference might be an effect of the slightly different rear wheel wake observed in Fig. 11. For W, a larger base drag is measured with a particularly lower pressure at the bottom right corner, close to the wheel. Figure 14 shows the vortex structures in the base plane. The vortices labelled 8 and 9 in Fig. 12b have propagated downstream. Comparing R and W, 9 is larger for W also in this plane. Its location approximately corresponds to the low-pressure region in Fig. 13c, presumably explaining the increased base drag.

3.3 Rim protectors on the closed rim

3.3.1 Front wheel flow

Compared to the open rim, a lower drag is measured for all tyres with the closed rim. For the reference and the low rim protector, the decrease is approximately $0.008 C_D$, whereas it is $0.021 C_D$ for the wide rim protector, demonstrating a strong interaction between the tyre and rim.

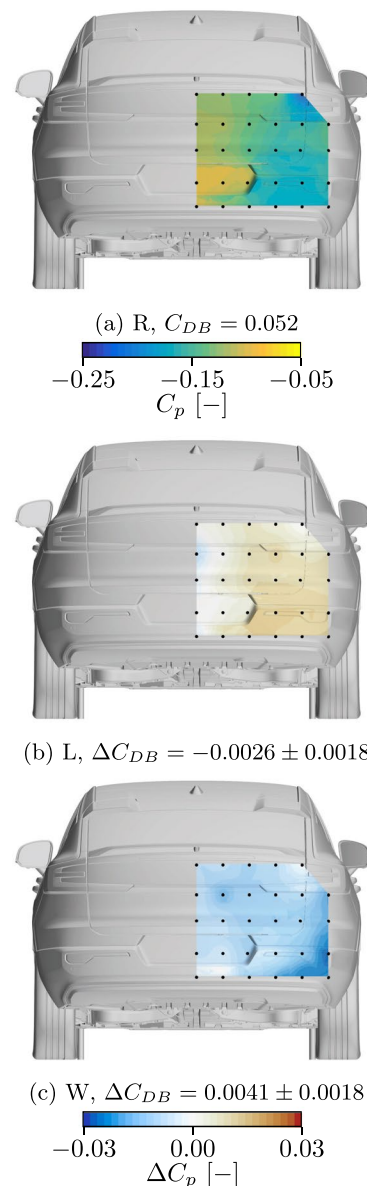


Fig. 13 Base pressure for R and base pressure deltas for L and W with the open rim. The base drag corresponds to a full vehicle

Figure 15 shows Γ_2 and total pressure in the FW x plane. Compared to the open rim (Fig. 8), the general trend for all three tyres is that the closed rim produces a smaller outer contact patch vortex (B) and a less pronounced C_{out} . Vortex D is also smaller which is in accordance with it being driven by the rim flow, as suggested by Wäschle (2007). Due to the convex rim cover, the wake is pushed outwards, resulting in a larger low-energy region in between B and F.

Comparing R and L, there is a small difference in C_{out} which reduces the upwash into the wheelhouse, giving a

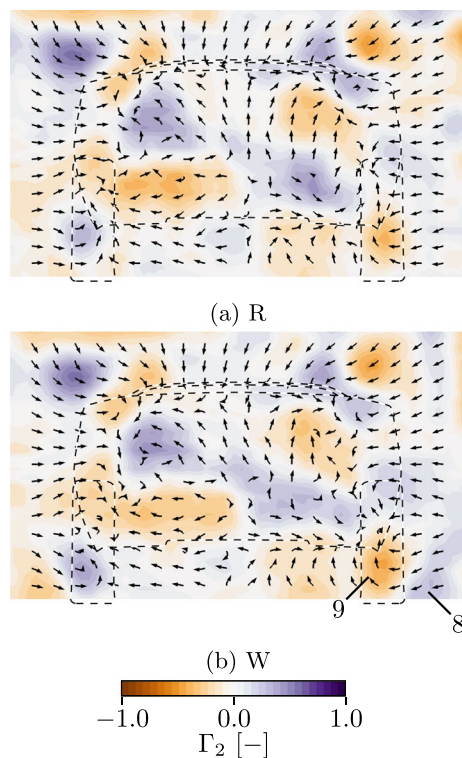


Fig. 14 Vortex structures with the open rim in the base plane. The dashed lines mark the outline of the vehicle base and rear wheels

slightly smaller upper separation (F) for L. With W, the B and D vortices are enlarged. However, the increase is less than for the open rim, explaining why the drag delta is much smaller (Fig. 7). Furthermore, C_{in} is shifted down and outwards, and C_{out} is not visible, resulting in more outwash. Comparing the outwash in the FW z plane (Fig. 16), W gives a larger wake with more losses. These changes are similar to those observed for the open rim. The difference in wake direction between R and W is, however, smaller with the closed rim.

Comparing the y -component of velocity between open and closed rims for the reference tyre, the main differences in FW x are found around the altered contact patch separation, Figs. 10a and 17a. In FW y , the convex rim cover results in more outflow over the upstream half of the closed rim (10). With the flow staying attached along the closed rim, the region of $v_y \approx 0$, created by the wide rim protector at the downstream transition between the tyre and rim, more clearly follows the circular shape (3).

3.3.2 Rear wheel flow

With the closed rim, the flow at the rear wheel is similar for all tyres, Fig. 18. As observed in Fig. 16, the front wheel

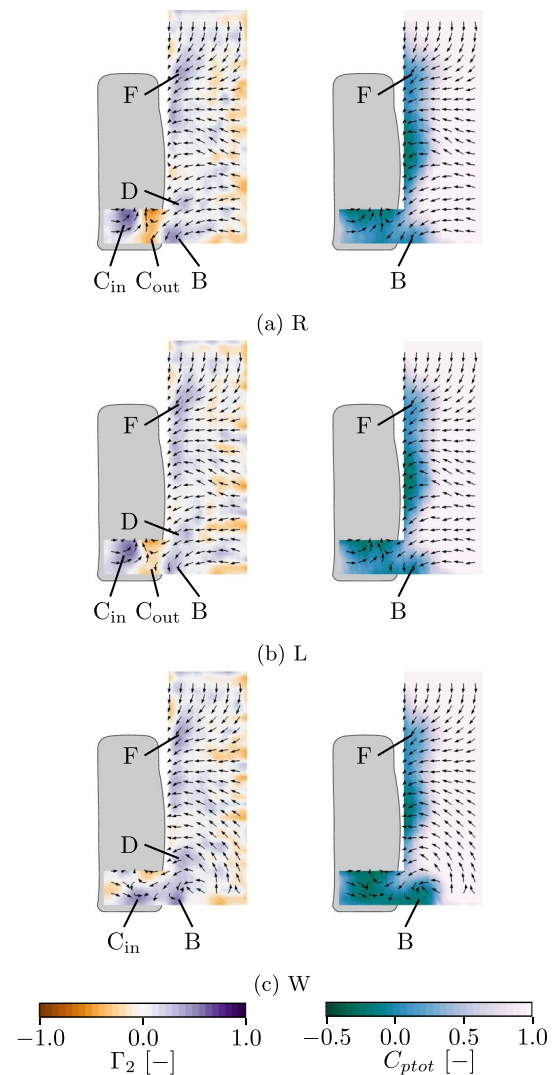


Fig. 15 Flow field measurements in the FW x plane for the three tyres with the closed rim

outwash did not increase as much with W on the closed rim as on the open rim. Hence, the low-energy region labelled 7 in Fig. 11c is not present in Fig. 18c, indicating that front wheel wake shields the rear wheel similarly for all tyres on the closed rim.

Comparing the base pressures (Fig. 19), the base drag is $0.003 C_{DB}$ less with the closed than with the open rim for R. Similar to the open rim, a small, homogeneous, pressure increase is obtained for L. With W, the base pressure is almost identical to R, strengthening the theory that the base pressure with the open rim was altered by the strong inflow downstream of the rear wheel.

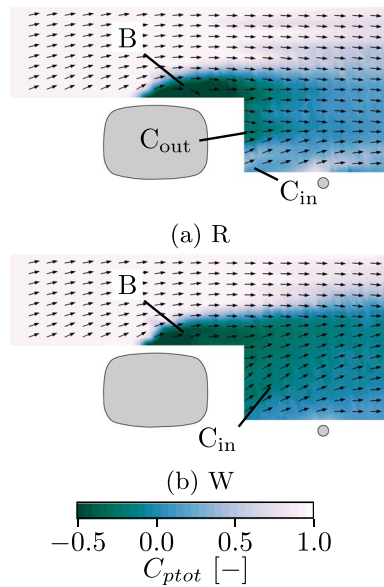


Fig. 16 Flow field measurements in the FW z plane with the closed rim. For reference, the outline of the mounting strut is indicated

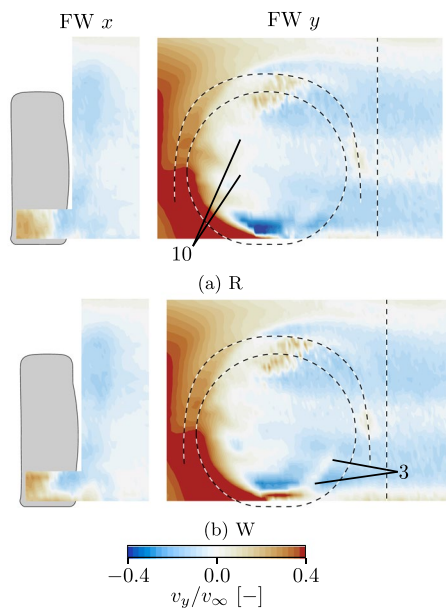


Fig. 17 Normalised spanwise velocity in the planes FW x and FW y for the closed rim. Positive values correspond to flow out from the vehicle. The dashed lines in FW y mark the outline of the wheel and wheelhouse as well as the location of the FW x plane

4 Conclusions

This work investigated the effects of geometrical modifications to the transition region between the rim and tyre on the flow field around a passenger vehicle. The comparison was performed using the same tyre profile, adding either a

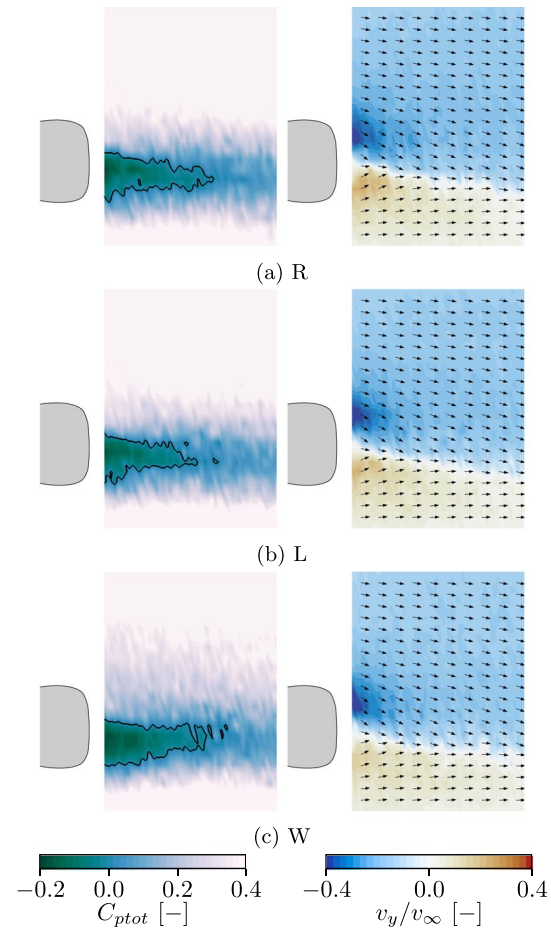


Fig. 18 Flow field measurements in the RW z plane with the closed rim. Isolines are drawn for $C_{ptot} = 0$

low or a wide rim protector, and two rim configurations. The measured force deltas were analysed using flow field and surface pressure measurements.

The addition of a low rim protector resulted in no drag difference with the open rim and a slight decrease with the closed rim. Apart from a small increase in the base pressure, the flow fields of the low rim protector were similar to the reference tyre.

With the wide rim protector, a drag increase of $0.017 C_D$ was measured on the open rim. For the closed rim, the penalty was only $0.003 C_D$. This reaffirms that there are strong interactions between the rim and the tyre. The drag increase with the wide rim protector was explained by larger outer contact patch (B) and rim (D) vortices at the front wheel. The front wheel wake was also larger and more outwash dominated, reducing the shielding of the rear wheel. This resulted in a decreased base pressure, further contributing to the higher drag.

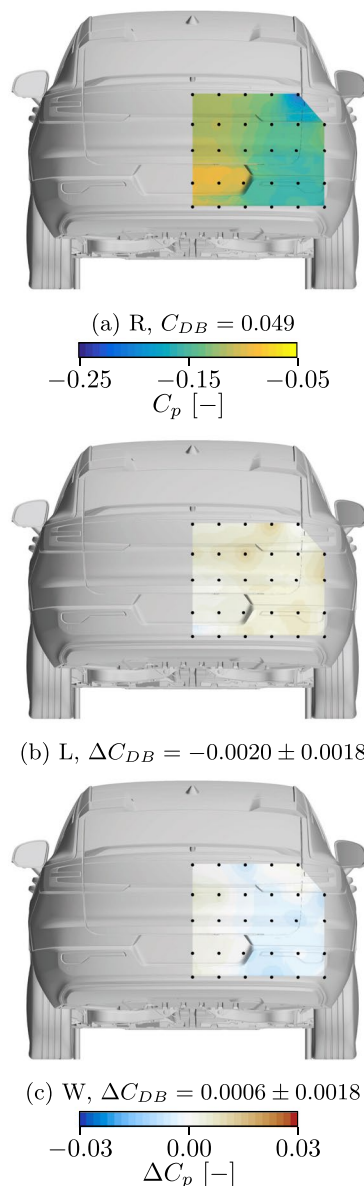


Fig. 19 Base pressure for R and base pressure deltas for L and W with the closed rim. The base drag corresponds to a full vehicle

Acknowledgements The authors would like to thank Pirelli tyre SpA, particularly Dr. Luca Camosi, for supplying the prototype tyres and the corresponding deformed CAD models. Numerical simulations were performed during the pre-study. The computations were enabled by resources provided by the Swedish National Infrastructure for Computing (SNIC), partially funded by the Swedish Research Council through grant agreement no. 2018-05973.

Author contributions EJ helped in conceptualisation, methodology, software, validation, formal analysis, investigation, data curation, writing—original draft, writing—review and editing and visualisation. FFS helped in conceptualisation, formal analysis, writing—original draft, writing—review and editing and visualisation. MU helped in conceptualisation, resources, writing—review and editing, supervision, project administration and funding acquisition. SS helped in

conceptualization, resources, writing—review and editing, supervision and funding acquisition.

Funding Open access funding provided by Chalmers University of Technology. This work is funded by the Swedish Energy Agency Grant No. P49114-1.

Availability of data and materials The authors do not have permission to share data.

Declarations

Conflict of interest The authors have no conflict of interest to declare that are relevant to the content of this article.

Ethical approval Not applicable.

Open Access This article is licensed under a Creative Commons Attribution 4.0 International License, which permits use, sharing, adaptation, distribution and reproduction in any medium or format, as long as you give appropriate credit to the original author(s) and the source, provide a link to the Creative Commons licence, and indicate if changes were made. The images or other third party material in this article are included in the article's Creative Commons licence, unless indicated otherwise in a credit line to the material. If material is not included in the article's Creative Commons licence and your intended use is not permitted by statutory regulation or exceeds the permitted use, you will need to obtain permission directly from the copyright holder. To view a copy of this licence, visit <http://creativecommons.org/licenses/by/4.0/>.

References

- Aeroprobe corporation (2015) Standard Probes User Manual
- Barth T et al (2020) The Aerodynamics of the VW ID.3 Electric Car. *ATZ Worldw* 122(9):48–53. <https://doi.org/10.1007/s38311-020-0270-5>. (ISSN: 2192-9076. Visited on 2024-01-25)
- Brandt A et al (2019) The effects of wheel design on the aerodynamic drag of passenger vehicles. *SAE Int J Adv Curr Pract Mobil* 1(3):1279–1299. <https://doi.org/10.4271/2019-01-0662>. (ISSN: 2641-9637. Visited on 2020-04-07)
- De Gregorio F, Visingardi A (2020) Vortex detection criteria assessment for PIV data in rotorcraft applications. *Exp Fluids* 61(8):179. <https://doi.org/10.1007/s00348-020-03012-7>. (ISSN: 1432-1114. Visited on 2023-05-15)
- Graftieaux L, Michard M, Grosjean N (2001) Combining PIV, POD and vortex identification algorithms for the study of unsteady turbulent swirling flows. *Meas Sci Technol* 12(9):1422–1429. <https://doi.org/10.1088/0957-0233/12/9/307>. (ISSN: 0957-0233. Visited on 2022-08-23)
- Gray M et al (2019) Improved methodology for realistic representation of rotating wheels in CFD applications. *Progress in Vehicle Aerodynamics and Thermal Management*. Stuttgart
- Hobeika T, Sebben S (2018) Tyre pattern features and their effects on passenger vehicle drag. *SAE Int J Passeng Cars Mech Syst* 11(5):401–413. <https://doi.org/10.4271/2018-01-0710>. (ISSN: 1946-4002. Visited on 2020-04-02)
- Josefsson E (2022) Tyre aerodynamics of passenger vehicles. Licentiate Thesis. Chalmers University of Technology
- Josefsson E et al (2022) Investigation of tyre pattern effect on the aerodynamics of a passenger vehicle. *J Fluids Eng*. <https://doi.org/10.1115/1.4054851>

- Josefsson E, Sebben S, Urquhart M (2023) Characterisation of the flow around passenger vehicle wheels with varying tyre profiles. *Int J Heat Fluid Flow*. <https://doi.org/10.1016/j.ijheatfluidflow.2023.109191>
- Koitrand S, Gaylard A, Fiet GO (2015) An investigation of wheel aerodynamic effects for a saloon car. In: *Proceedings of the 10th FKFS-conference*. pp 240–255
- Landström C et al (2012) Aerodynamic effects of different tire models on a sedan type passenger car. *SAE Int J Passeng Cars Mech Syst* 5(1):136–151. <https://doi.org/10.4271/2012-01-0169>. (ISSN: 1946-4002. Visited on 2021-11-29)
- Ljungskog E, Sebben S, Broniewicz A (2019) Inclusion of the physical wind tunnel in vehicle CFD simulations for improved prediction quality. *J Wind Eng Ind Aerodyn*. <https://doi.org/10.1016/j.jweia.2019.104055>
- Mercker E et al (1991) On the aerodynamic interference due to the rolling wheels of passenger cars. *SAE Trans* 100:460–476 (ISSN: 0096-736X. Visited on 2021-10-06)
- Mlinaric P (2007) Investigation of the influence of tyre deformation and tyre contact patch on CFD predictions of aerodynamic forces on a passenger car. MA thesis. Gothenburg: Chalmers University of Technology
- Parfett A, Babinsky H, Harvey JK (2022) A study of the time-resolved structure of the vortices shed into the wake of an isolated F1 car wheel. *Exp Fluids* 63(7):116. <https://doi.org/10.1007/s00348-022-03458-x>. (ISSN: 1432-1114. Visited on 2022-08-16)
- Radovic R, Salehi F, Diasinos S (2023) A detailed numerical study on aerodynamic interactions of tandem wheels on a generic vehicle. *Fluids* 8(10):281. <https://doi.org/10.3390/fluids8100281>. (ISSN: 2311-5521. Visited on 2024-01-23)
- Reiß J et al (2020) Experimental and numerical investigations on isolated, treaded and rotating car wheels. *SAE Technical Paper* 2020-01-0686 (2020-04). <https://doi.org/10.4271/2020-01-0686>
- Schnepf B, Tesch G, Indinger T (2015) On the influence of ride height changes on the aerodynamic performance of wheel designs. *Int J Autom Eng* 6(1):23–29. https://doi.org/10.20485/jsaeijae.6.1_23
- Schuetz TC (2015) *Aerodynamics of road vehicles*, 5th edn, SAE International, Warrendale 2015-12. <https://doi.org/10.4271/r-430>
- Sterken L et al (2014) Effect of the traversing unit on the flow structures behind a passenger vehicle. In: *IMEchE International vehicle aerodynamics conference*. Loughborough
- Sternéus J, Walker T, Bender T (2007) Upgrade of the Volvo cars aerodynamic wind tunnel. *SAE Technical Paper* 2007-01-1043 (2007-04). <https://doi.org/10.4271/2007-01-1043>
- Wäschle A (2007) The influence of rotating wheels on vehicle aerodynamics - numerical and experimental investigations. *SAE Technical Paper* 2007-01-0107 (2007-04). <https://doi.org/10.4271/2007-01-0107>
- Wickern G, Zwicker K, Pfadenhauer M (1997) Rotating Wheels - Their Impact on Wind Tunnel Test Techniques and on Vehicle Drag Results. *SAE Trans*. <https://doi.org/10.4271/970133>
- Wittmeier F et al (2014) Model scale based process for the development of aerodynamic tire characteristics. *SAE Technical Paper* 2014-01-0585 (2014-04). <https://doi.org/10.4271/2014-01-0585>
- Wittmeier F et al (2013) Tyre development from an aerodynamic perspective. *ATZ Worldw* 115(2):42–48. <https://doi.org/10.1007/s38311-013-0022-x>. (ISSN: 2192-9076. Visited on 2022-06-29)

Publisher's Note Springer Nature remains neutral with regard to jurisdictional claims in published maps and institutional affiliations.